Sound & Vibration 2025, 59(5), 3788.
doi: https://doi.org/10.59400/sv3788

Article

Coupling vibration analysis for inspection robot landing on high voltage transmission line

Xiaodong Zhang[1,2], Haiming Shen[1,3,*], Ahmad Bala Alhassan[4], Haibo Xu[1,2]

[1] School of Mechanical Engineering, Xi'an Jiaotong University, Xi'an 710049, China
[2] Shaanxi Key Laboratory of Intelligent Robot, Xi'an Jiaotong University, Xi'an 710049, China
[3] College of Mechanical and Electrical Engineering, Shihezi University, Shihezi 832003, China
[4] School of Mechanical Engineering, Chulalongkorn University, Bangkok 10330, Thailand
*** Corresponding author:** Haiming Shen, shenhaiming13@163.com

CITATION

Zhang X, Shen H, Alhassan AB, et al. Coupling vibration analysis for inspection robot landing on high voltage transmission line. Sound & Vibration. 2025; 59(5): 3788. https://doi.org/10.59400/sv3788

ARTICLE INFO

Received: 24 August 2025
Revised: 2 October 2025
Accepted: 12 October 2025
Available online: 27 October 2025

Abstract: When the high-voltage transmission line inspection robot (HVTIR) with a landing gripper lands during flight, the rigid-flexible coupling vibration between the HVTIR and the transmission line severely undermines landing stability. Therefore, investigating the HVTIR-line coupling vibration characteristics during landing is critical for achieving stable landing control. Ignoring wind and airflow disturbances, this study analyzes the input-output characteristics of the HVTIR-line coupled vibration system and the interaction forces between adjacent components, then derives their motion differential equations. The transmission line is decomposed into a model of multiple unit-length Euler beams hinged by stiffness and damping, and a stiffness-damping coupling model for the gripper-line contact force is established. On this basis, a mass-stiffness-damping model of the HVTIR-line system is constructed to obtain its rigid-flexible coupling vibration characteristics. A vibration test system is built using an acceleration sensor wireless acquisition system, and the vibration characteristic curves of the HVTIR gripper and transmission line are obtained and compared with the theoretical simulation results. The results show that the experimental and simulation data share the same trend, with a maximum error of no more than 13.64%; the interquartile range increment between them ranges from 10.67% to 18.26%, verifying the model's scientific validity. This study optimizes the transmission line modeling method to ensure calculation accuracy and real-time analysis efficiency, and constructs a novel HVTIR-line rigid-flexible coupling model, which provides a theoretical basis for smooth and rapid HVTIR landing control.

Keywords: landing gripper; HVTIR landing on the line; rigid-flexible coupled vibrations; HVTIR–line dynamics; multibody modeling

1. Introduction

With the trend of the world population towards the concentration of metropolises and the regional restrictions of wind power, solar power, nuclear power, and other electric power, remote power transmission is becoming increasingly significant. High-voltage transmission lines have become the arteries of infrastructure construction and social development in many countries in the world. Intelligent, efficient, and safe patrol inspection of high-voltage transmission lines has become an urgent problem for the development of the power industry [1–3]. There are two main types of HVTIR. One is to use unmanned aerial vehicles to achieve rapid inspection of transmission lines, but

due to the limitation of safety distance, it is impossible to carry out close and accurate inspection [4–6]. The other is to achieve close inspection through a robot with arms sliding on the line; the inspection accuracy is high, but it is difficult to get up and down the transmission line, and the efficiency of climbing over large obstacles and the tower is low [7–9]. Therefore, it is extremely important to study the high-voltage transmission line composite mode inspection robot that can meet the requirements of quickly getting up and down the line, crossing the large obstacles, and the tower [10–12]. Our team has developed an HVTIR with the fly-climbing-sliding composite function, which solved the above problems [13]. The team studied the coupling effect between HVTIR and the transmission line during sliding. The study simplifies the transmission line into a string model to investigate the coupled vibration between HVTIR and the transmission line, which results in a large computational load. Based on vibration analysis, a control method for smooth motion was studied.

During the transition from flight state to online mode of the fly-climbing-sliding HVTIR, its smooth landing on the line is the key to realizing the transition. The change law of the rigid-flexible coupling contact force between the HVTIR and the transmission line during the flight landing is the basis for controlling the landing stability. There is currently little research on the coupling force of multi-modal inspection robots during flight and landing on transmission lines. The following analyzes the research status of the coupling effect between the aerial manipulator and targets.

In some studies, the coupling force between the actuator of the aerial manipulator and the target is not studied in the process of studying the control of the actuator. It is directly adjusted by the motion of the UAV. In Ye et al. and Luna et al. [14, 15], the mutual distance is measured by the visual perception to achieve control. In Yigit et al. and Ji et al. [16,17], the mutual distance is measured through a displacement sensor and visual perception to achieve control. These methods directly use a distance sensor or a visual sensor to adjust and control the coupling force between the actuator of the aerial manipulator and the target, ignoring the coupling characteristics of contact force, and the control accuracy is not high. Especially for the HVTIR in the process of landing, the coupling force between the actuator of the robot and the transmission line is large, and the coupling force has a direct impact on the stability of the landing line.

At present, the research on the coupling force between the actuator of an aerial manipulator and the target mainly includes the following:

Some studies either ignore the coupling force characteristics between the aerial manipulator and the target or treat the coupling contact force as a rigid connection. In Hamaza et al. and Zhang et al. [18, 19], the research treats the coupling force between the actuator of the aerial manipulator and the target as a rigid action, and solves the contact force through rotor lift and coordinate system transformation.

Some studies take the target as a rigid body, and the contact force is simplified as a group of stiffness and damping. In Khanmirza et al. and Meng et al. [20, 21], the contact force between the aerial manipulator and the object is simplified as a single stiffness-damping, and the change law of the coupling force between them is studied, but the target object is a rigid body.

In some studies, the coupling contact force can be transformed into a flexible arm for processing. In Wang et al. [12], the connecting rod between the aerial manipulator and the tip mass block is treated as a flexible beam. Through the study of the vibration characteristics of the mass block and the beam, the impact on the position and attitude of the flying robot during flight is solved.

According to the above research, the rigid-flexible coupling law between the aerial manipulator and the flexible target has not been studied yet. Therefore, it is very innovative to construct a rigid-flexible coupling model between the robot and flexible target, study their vibration characteristics, and obtain the interaction law of the contact force.

In this study, the rigid-flexible coupling vibration of the HVTIR and the flexible transmission line during the landing process is taken as the research object, the system model is established, the law of the coupling vibration between the HVTIR and the line is found, and the experimental system is constructed to verify the rationality of the model analysis. This provides theoretical support for the accurate control of the smooth landing of the inspection robot.

2. Methods

2.1. Analysis of the research object

The laboratory independently designed and developed a high-voltage transmission line composite mode HVTIR combining flight mode and online inspection mode [22,23]. The structure of the HVTIR is composed of a four-rotor aircraft and two climbing and sliding mechanical arms. The structure is shown in **Figure 1**.

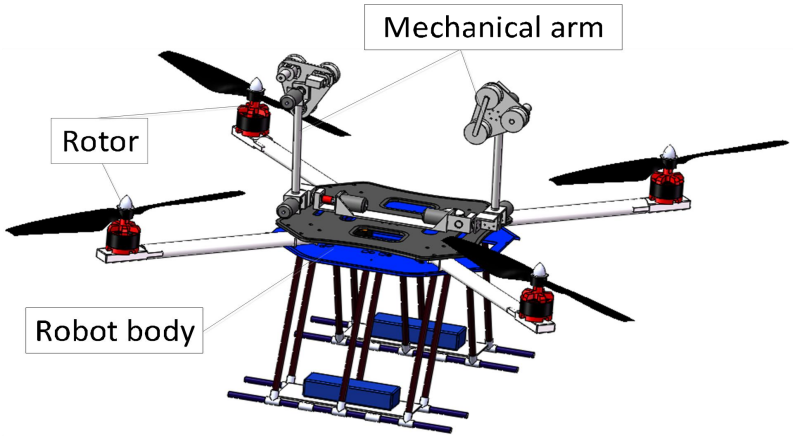

Figure 1. Structure diagram of the HVTIR.

In the power system, high voltage transmission lines have single conductor, double split, triple split, and quadruple split, and no split conductor is required below 110 KV. However, 220 KV, 330 KV, 500 KV, 1000 KV, and other voltage lines will use split conductors in order to suppress corona discharge, optimize line parameters, and improve the transmission capacity of the line and the stability of the power system operation. The anti-vibration hammer, spacer, anti-dance device, and other hardware between the split conductors also have a complex impact on the vibration of the

transmission line [24, 25]. These structures are shown in **Figure 2**. This study is a simplified model, and a single conductor is selected as the research object.

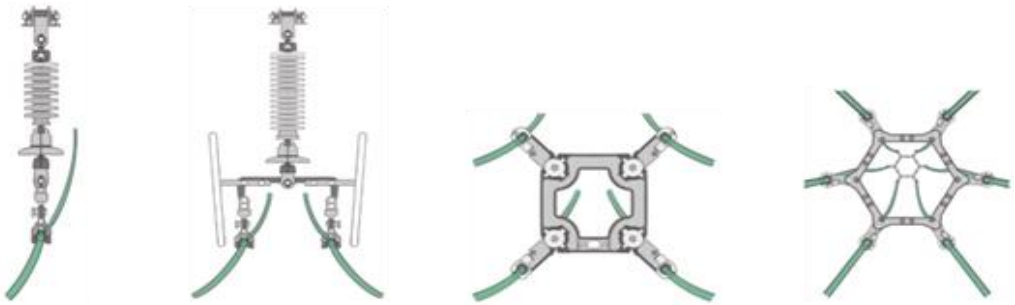

(a) **(b)** **(c)** **(d)**

Figure 2. Schematic diagram of a split conductor of a high-voltage transmission line. **(a)** single bundle conductor; **(b)** two bundle conductor; **(c)** four bundle conductor; **(d)** six bundle conductor.

The robot flies close to the power transmission line, the gripper at the front of the mechanical arm catches the power transmission line, and the rotor decelerates to a stop to realize the landing function. The process of the robot getting close to the high-voltage transmission line and landing on the transmission line is shown in **Figure 3**.

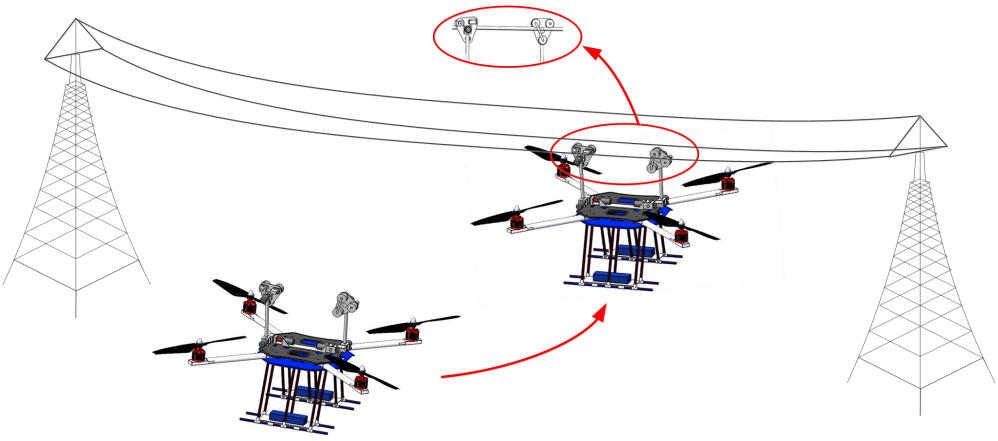

Figure 3. Schematic diagram of HVTIR landing line.

Due to the large load of the HVTIR in this design, the flight parts adopt a large wheelbase four-rotor with a blade diameter of 762 mm and a wheelbase diameter of 1380 mm. (In engineering, UAVs with wheelbase diameters greater than 1000 mm are called large wheelbase UAVs) [23]. In the process of landing, the HVTIR with a large wheelbase and a heavy load has a large impact on the transmission line, which can easily cause the coupling time-varying force between the transmission line and the HVTIR, affecting the stability and efficiency of landing. In this paper, a vibration tactile sensing method is proposed to obtain the change law of the coupling force between the HVTIR and the transmission line. That is, the change law of the contact force between the HVTIR and the transmission line is obtained by studying the coupling vibration characteristics between the transmission line and the HVTIR.

The vibration source of flying HVTIR mainly comes from its rotor vibration. The rotor vibration of a large wheelbase UAV can be divided into rotary vibration,

pulse vibration, and bandwidth vibration. The rotary vibration is mainly generated on the blade, with low frequency; pulse vibration is mainly caused by the eddy current interference of the blade, and its high frequency will bring high frequency noise interference; bandwidth vibration is caused by the uneven air flow on the blade, and the vibration amplitude and energy are very small, so the rotor rotating vibration has the greatest impact on the attitude of the UAV [23]. Because the UAV rotor steering gear uses a DC motor, the influence of its vibration can be ignored. The rotor rotating vibration mainly comes from the rotor dynamic unbalance. If the higher-order array of vibration signals is ignored, the rotor vibration frequency is the same as the rotor rotating frequency. The rotor rotating vibration can be equivalent to the force T acting on the rotor. Because the horizontal component of vibration has little influence on the position and posture of the HVTIR gripper, it can be ignored, so the force is decomposed in the coordinate system, and only the vertical component needs to be retained.

The vertical component is Equation (1):

$$T_Z = A\cos(\omega t + \gamma) \tag{1}$$

Where, A is the magnitude of force, ω is the angular velocity of rotor rotation, γ is the initial phase of vibration, and is related to the position of the rotor before starting. According to engineering practice, A = 1 N. The rotor speed of this design is 1500–3600 rpm, and the vibration frequency is about 25–60 HZ, which belongs to low-frequency interference.

In the process of landing, the change of rotor speed will bring about the change of lift, which will cause the vibration of HVTIR system, that is, the rotor lift is the input source of system vibration; at the same time, the equivalent force of rotor rotating vibration is also the source of system vibration; ignore the position drift of the HVTIR in the air caused by the positioning and navigation system error; then the input of the whole vibration system from the rotor component to the wheel claw is the sum of the rotor lift force F and the equivalent force of the vibration on it.

In the process of HVTIR landing, the transmission line will vibrate after being impacted by the impact force of HVTIR landing. Because the transmission line has a long span and a large weight, its own vibration is also large. The coupling force between the transmission line and the HVTIR gripper can be obtained through the vibration characteristics of the contact between the transmission line and the wheel claw.

In the process of landing, the interaction between the HVTIR gripper and the transmission line is the key index that affects the stability and efficiency of the HVTIR landing. The vibration tactile sensing is used to obtain the coupling force, so the vibration characteristics of the robot-line coupling in the whole landing process are the output of the system.

The mass-stiffness-damping method is used to study the vibration characteristics of the system's HVTIR and transmission line coupling, grasp its vibration rules, and provide a theoretical basis for the precise control of the HVTIR's smooth and efficient landing.

2.2. Coupled vibration model

The mass-stiffness-damping multi-degree-of-freedom model is used to simulate the state of the robot-line coupling system of the HVTIR when landing. At this time, the HVTIR vertical deceleration flight. The coordinate system is as shown in **Figure 4**. The origin of the coordinate system is at the center of the HVTIR body, and the Z axis is vertically upward. In order to analyze the vibration characteristics of each component, the HVTIR is dissected and analyzed along the three directions of AC, BD, and EF.

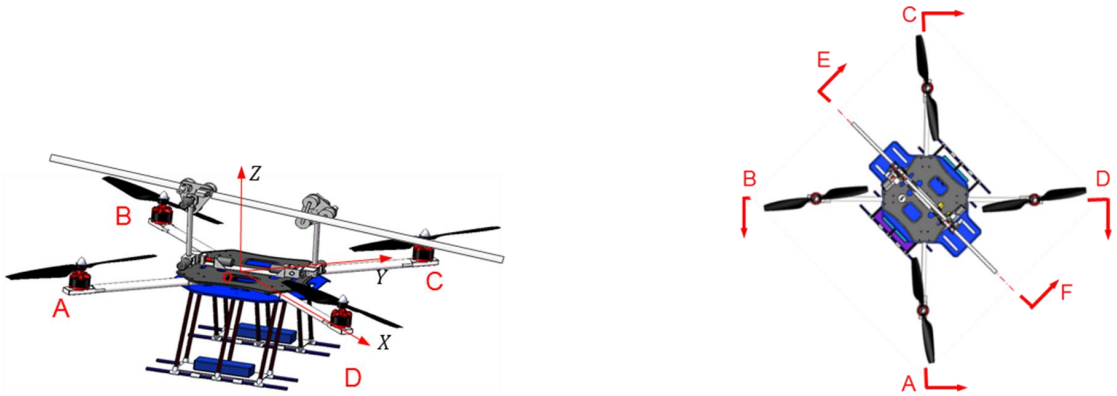

(a) Coordinate system of HVTIR and line coupling. **(b)** Schematic diagram of HVTIR section direction.

Figure 4. Coordinate system and sectional sketch of HVTIR landing flight.

Transmission lines and towers do not exist independently. As shown in **Figure 5**, they are connected with multiple transmission lines, so the vibration between adjacent transmission lines and towers has a coupling effect. In order to simplify the complexity of the study, this paper only studies the coupled vibration of the transmission line between the two towers. And the model temporarily does not consider the influence of wind power.

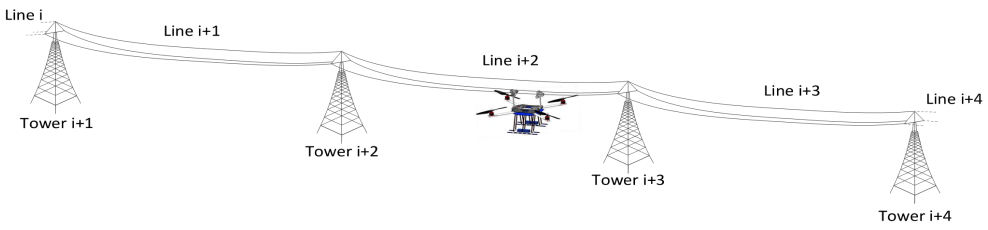

Figure 5. Transmission line and tower system.

As shown in **Figure 6**, the high-speed rotation of the four rotors produces vertical upward lift (F_1, F_2, F_3, F_4) and rotary vibration of the rotors. The rotary vibration of the rotor can be equivalent to the force (T_{Z1}, T_{Z2}, T_{Z3}, T_{Z4}) in the vertical direction. Then F_1, F_2, F_3, F_4, and T_{Z1}, T_{Z2}, T_{Z3}, T_{Z4} are the inputs of the vibration system, and the vibration of the landing grippers is the output of the system.

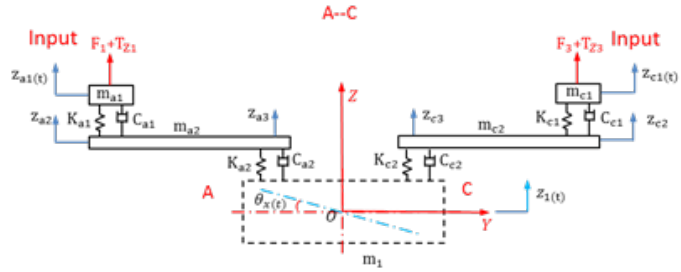

(**a**) Vibration model of HVTIR in A–C section direction.

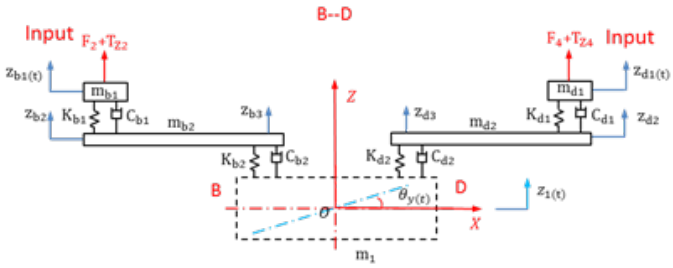

(**b**) Vibration model of HVTIR in B–D section direction.

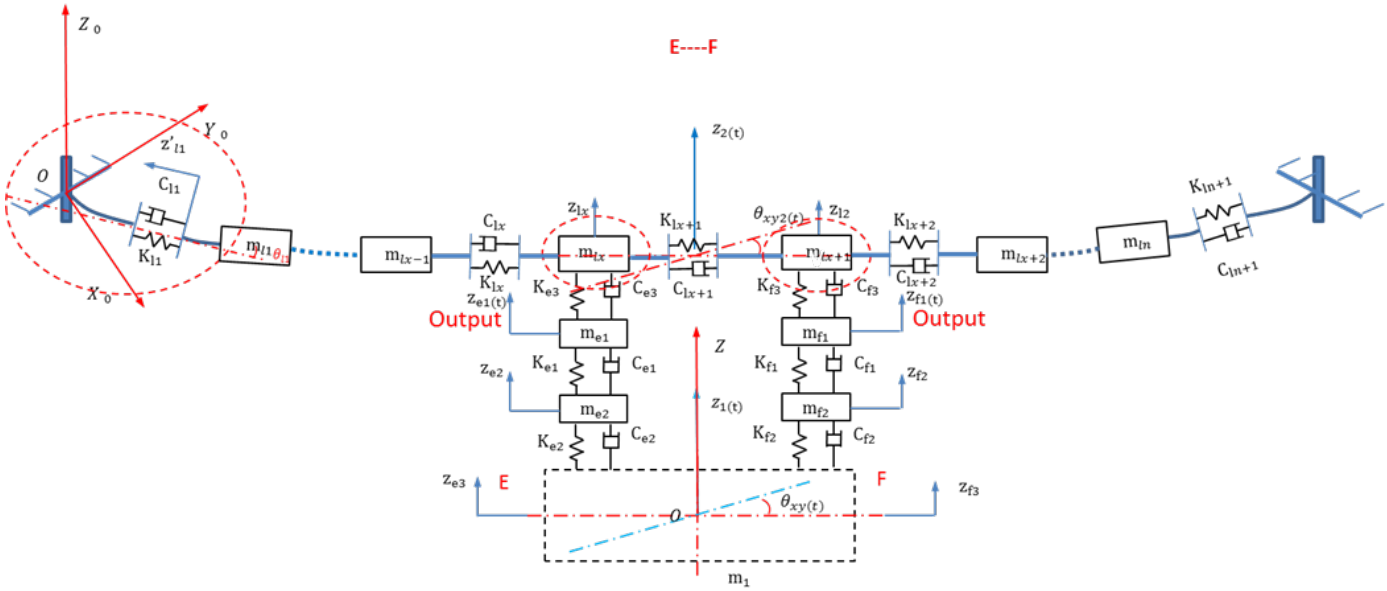

(**c**) Vibration model of HVTIR in the E–F section direction.

Figure 6. Vibration model of HVTIR and the line in landing flight.

$$T_{Z1/Z2/Z3/Z4} = A\cos(\omega_{Z1/Z2/Z3/Z4}t + \gamma_{Z1/Z2/Z3/Z4}) \tag{2}$$

$T_{Z1/Z2/Z3/Z4}$ are the vertical equivalent forces of the rotational vibration of the four rotors, as shown in Equation (2); $\omega_{Z1/Z2/Z3/Z4}$ are the rotational angular velocity of the four rotors; $\gamma_{Z1/Z2/Z3/Z4}$ are the initial phase of the rotational vibration of the four rotors.

$$F_{1/2/3/4} = C_F\rho(\frac{N_{1/2/3/4}}{60})D_p^4 \tag{3}$$

$F_{1/2/3/4}$ are the vertical lift of four rotors, as shown in Equation (3); C_F is the dimensionless lift coefficient; D_p is the rotor diameter (m); ρ is the air density of the flight environment (kg/m^3), which is related to flight altitude h and temperature T_t.

$$\rho = \frac{273P_a}{101325(273 + \mathrm{T}_t)}\rho_0 \tag{4}$$

ρ_0 = 1.293 kg/m^3 is the standard atmospheric density, as shown in Equation (4); Pa is the atmospheric pressure (p_a).

$\mathrm{N}_{1/2/3/4}$ are the four rotor speeds (rpm), as shown in Equation (5).

$$N_{1/2/3/4} = \frac{\omega_{1/2/3/4}}{2\pi} \tag{5}$$

In **Figure 6**, m_{a1}, m_{b1}, m_{c1}, and m_{d1} are the mass centers simplified from the blades to the rotorcraft arms; and the parameters K_{a1}, K_{b1}, K_{c1}, K_{d1}, and C_{a1}, C_{b1}, C_{c1}, C_{d1} are their corresponding stiffness and damping. m_{a2}, m_{b2}, m_{c2} and m_{d2} are the mass centers simplified from the mass of each paddle arm to the connection point of the HVTIR body; $Z_{a2}(t)$, $Z_{b2}(t)$, $Z_{c2}(t)$, $Z_{d2}(t)$ are its vertical displacements from the equilibrium position and the parameters K_{a2}, K_{b2}, K_{c2}, K_{d2} and C_{a2}, C_{b2}, C_{c2}, C_{d2} are the corresponding stiffness and damping. The HVTIR body can be simplified into a compact cuboid with a mass of m_B, K_B and C_B are its corresponding stiffness and damping, its center of gravity is G, the initial position of static balance of G is the HVTIR coordinate origin O. The vertical displacement $q_1(t)$ of the body is the displacement of G, the center of gravity, from the static equilibrium position, $\theta_x(t)$ is the rotation angle of the body around the X axis, $\theta_y(t)$ is the rotation angle of the body around the Y axis. A, B, C, and D are the connection points between the rotorcraft arms and the HVTIR body. E and F are the connection points between the landing gripper manipulators and the HVTIR body. m_{e2} and m_{f2} are the centroids simplified from the E/F point to the HVTIR gripper. $Z_{e2}(t)$ and $Z_{f2}(t)$ are their vertical displacement from the balance position, parameters K_{e2}, K_{f2}, and C_{e2}, C_{f2} are the corresponding stiffness and damping. m_{e1}, m_{f1} are the centroid simplified from the mass of the gripper at the top of the manipulator, $Z_{e1}(t)$, $Z_{f1}(t)$ are their vertical displacement from balance position, parameters K_{e1}, K_{f1}, and C_{e1}, C_{f1} are the corresponding stiffness and damping.

In the high voltage transmission line vibration system, the conductor span between two poles and towers is tens of meters, or even hundreds of meters. In this study, the conductor with a span of 100 m is selected as the research object, and the conductor is divided into n parts. The stiffness and damping between the ends of the transmission line and the poles and towers are K_{l1}, C_{l1}, K_{ln+1}, C_{ln+1}, and the mass of the transmission line per meter is ml. The slight error caused by the bending of the transmission line is ignored. The stiffness between the transmission lines per meter is K_l, and the damping is C_l. The included angle between the transmission line and the horizontal caused by suspension and vibration is $\theta_{xy}(t)$.

According to D'Alembert's principle, the vibration differential equations of each part are listed from the four rotors of the HVTIR to the body of the HVTIR.

a) Vertical vibration differential equations of the four rotor components, as shown in Equation (6):

$$\begin{gathered} m_i\ddot{q}_{i1}(t) - c_{i1}(\dot{q}_{i1}(t) - \dot{z}_{i2}(t)) - k_{i1}(q_i(t) - z_{i2}(t)) + F_j + T_{Zj} - m_{a1}g = 0 \\ (\mathrm{i} = \mathrm{a}, \mathrm{j} = 1; \mathrm{i} = \mathrm{b}, \mathrm{j} = 2; \mathrm{i} = \mathrm{c}, \mathrm{j} = 3; \mathrm{i} = \mathrm{d}, \mathrm{j} = 4) \end{gathered} \tag{6}$$

b) Vertical vibration differential equations of four rotorcraft arms:

Because the rotorcraft arm is a carbon fiber tube with a length of 0.675 m, a diameter of 0.025 m, and a wall thickness of 0.002, and both ends are connected with the rotor components and the HVTIR body, respectively, it is treated as a beam with spring mass blocks connected at both ends here.

As shown in **Figure 7**, the inertia force of the beam element is $\rho A(y)dy\partial z^2(y,t)/\partial z^2$.

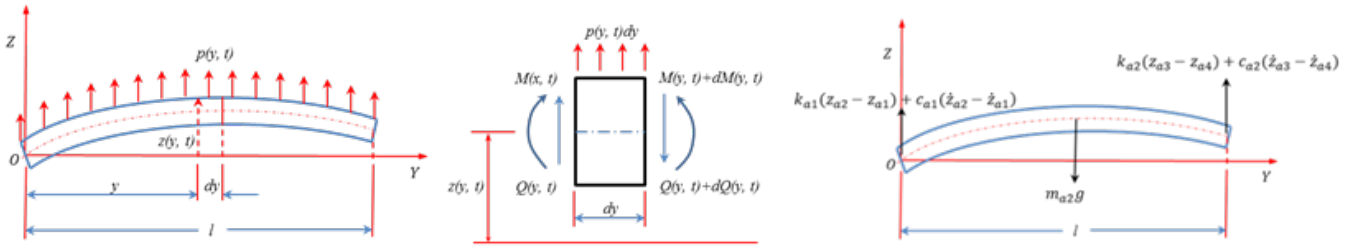

(**a**) Transverse vibration of a beam. (**b**) Force and bending of the micro segment. (**c**) Load of the whole beam.

Figure 7. Vibration analysis diagram of the boom.

Ignoring the influence of axial force, the relationship between bending moment and shear force is as shown in Equation (7):

$$Q = \frac{\partial M}{\partial y} \tag{7}$$

According to Euler-Bernoulli theory, the relationship between bending moment and deflection of the beam is as shown in Equation (8):

$$M(y,t) = EI(y)\frac{\partial z^2(y,t)}{\partial y^2} \tag{8}$$

From Equations (7) and (8), the vibration equation of the beam is as shown in Equation (9):

$$\begin{cases} Q(x,t) = \frac{\partial}{\partial y}(EI\frac{\partial z^2}{\partial y^2}) = a\,(kz + c\frac{\partial z}{\partial t}) \\ EI\frac{\partial z^2}{\partial y^2} = 0 \end{cases} \tag{8}$$

Because both ends of the beam are connected with spring damping, the end resistance and shear force are balanced, and the bending moment is zero.

The stress analysis of the boom is shown in **Figure 6**; its far-end a_2/c_2 /b_2/d_2 vibration equations are as shown in Equation (10):

$$\begin{cases} (EI\frac{\partial^4 z_{i2}}{\partial y^4} + \rho A\frac{\partial^2 z_{i2}}{\partial t^2})\Big|y = -\frac{\sqrt{2}}{2}l - 0.53 \;= \frac{k_{i1}(z_{i2}-z_{i1}) + c_{i1}(\dot{z}_{i2}-\dot{z}_{i1}) - [k_{i2}(z_{i3}-z_{i4}) + c_{i2}(\dot{z}_{i3}-\dot{z}_{i4})] - m_{i2}g}{l} \\ z_{i4} = z_1 + \frac{l}{2}sin\theta_j \\ \frac{\partial}{\partial y}(EI\frac{\partial^2 z_{i2}}{\partial y^2})\Big|y = -\frac{\sqrt{2}}{2}l - 0.53 \;= k_{i1}(z_{i2}-z_{i1}) + c_{i1}(\dot{z}_{i2}-\dot{z}_{i1}) \\ EI\frac{\partial^2 z_{i2}}{\partial y^2}\Big|y = -\frac{\sqrt{2}}{2}l - 0.53 \;= 0 \\ (i=a, j=x;\ i=c, j=x;\ i=b,\ j=y;\ i=d,\ j=y) \end{cases} \tag{10}$$

The vibration equation at the near-end $a_3/c_3/b_3/d_3$ are as shown in Equation (11):

$$\begin{cases} (EI\dfrac{\partial^4 z_{i3}}{\partial y^4}+\rho A\dfrac{\partial^2 z_{i3}}{\partial t^2})\left|y=-\dfrac{\sqrt{2}}{2}l\right. = \dfrac{k_{i1}(z_{i2}-z_{i1})+c_{i1}(\dot{z}_{i2}-\dot{z}_{i1})-[k_{i2}(z_{i3}-z_{i4})+c_{i2}(\dot{z}_{i3}-\dot{z}_{i4})]-m_{i2}g}{l} \\ z_{i4}=z_1+\dfrac{l}{2}sin\theta_j \\ \dfrac{\partial}{\partial y}(EI\dfrac{\partial^2 z_{i3}}{\partial y^2})\left|y=-\dfrac{\sqrt{2}}{2}l\right. = k_{i2}(z_{i3}-z_{i4})+c_{i2}(\dot{z}_{i3}-\dot{z}_{i4}) \\ EI\dfrac{\partial^2 z_{i3}}{\partial y^2}\left|y=-\dfrac{\sqrt{2}}{2}l\right. = 0 \\ (i=a,j=x;\ i=c,j=x;\ i=b,\ j=y;\ i=d,\ j=y) \end{cases} \tag{11}$$

c) Vibration differential equation of HVTIR body:

As shown in **Figure 8**, under the input excitation of rotor components, four vertical displacements, $Z_{a3}(t)$, $Z_{b3}(t)$, $Z_{c3}(t)$, and $Z_{d3}(t)$ are generated at four points A, B, C, and D of the HVTIR body, respectively. $\theta_x(t)$ is the rotation angle of the HVTIR body around the X axis. $\theta_y(t)$ is the rotation angle of the HVTIR body around the Y axis of the HVTIR body. Because the vibration angular displacement is small, $\theta_x(t)$ and $\theta_y(t)$ are as shown in Equations (12) and (13):

$$\theta_x(t)=\sin\theta_x(t)=\frac{z_{c3}(t)-z_{a3}(t)}{\sqrt{2}l} \tag{12}$$

$$\theta_y(t)=\sin\theta_y(t)=\frac{z_{d3}(t)-z_{b3}(t)}{\sqrt{2}l} \tag{13}$$

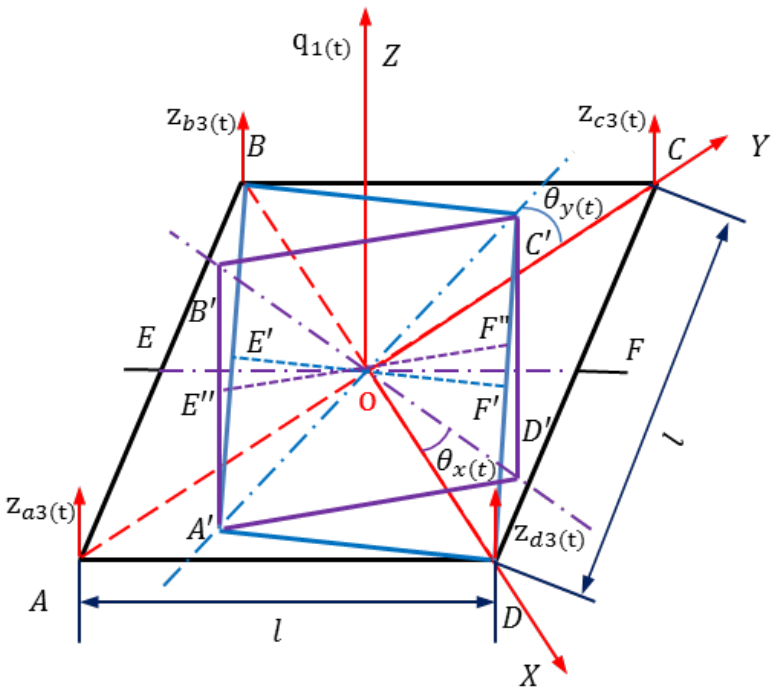

Figure 8. Motion modal analysis diagram of the HVTIR body.

From Equations (12) and (13), the input vertical displacement of four points A, B, C, and D of the HVTIR body can be obtained, as shown in Equations (14)–(17).

$$z_{a3}=q_1(t)-\frac{\sqrt{2}}{2}l\theta_x(t) \tag{14}$$

$$z_{b3} = q_1(t) - \frac{\sqrt{2}}{2} l\theta_y(t) \tag{15}$$

$$z_{c3} = q_1(t) + \frac{\sqrt{2}}{2} l\theta_x(t) \tag{16}$$

$$z_{d3} = q_1(t) + \frac{\sqrt{2}}{2} l\theta_y(t) \tag{17}$$

At the same time, the output vertical displacement of E and F points of the HVTIR body can also be obtained, as shown in Equations (18) and (19).

$$z_{e3} = q_1(t) - \frac{\sqrt{2}}{4} l(\theta_x(t) + \theta_y(t)) \tag{18}$$

$$z_{f3} = q_1(t) + \frac{\sqrt{2}}{4} l\,(\theta_x(t) + \theta_y(t)) \tag{19}$$

Vertical vibration differential equation of the HVTIR body is as shown in Equation (20):

$$\begin{aligned} &m_1\ddot{q}_1(t) + c_{a2}(\dot{z}_{a2} - \dot{q}_1(t) + \frac{\sqrt{2}}{2} l\dot{\theta}_x(t)) + k_{a2}(z_{a2} - q_1(t) + \frac{\sqrt{2}}{2} l\theta_x(t)) \\ &+c_{b2}(\dot{z}_{b2} - \dot{q}_1(t) + \frac{\sqrt{2}}{2} l\dot{\theta}_y(t)) + k_{b2}(z_{b2} - q_1(t) + \frac{\sqrt{2}}{2} l\theta_y(t)) \\ &+c_{c2}(\dot{z}_{c2} - \dot{q}_1(t) - \frac{\sqrt{2}}{2} l\dot{\theta}_x(t)) + k_{c2}(z_{c2} - q_1(t) - \frac{\sqrt{2}}{2} l\theta_x(t)) \\ &+c_{d2}(\dot{z}_{d2} - \dot{q}_1(t) - \frac{\sqrt{2}}{2} l\dot{\theta}_y(t)) + k_{d2}(z_{d2} - q_1(t) - \frac{\sqrt{2}}{2} l\theta_y(t)) \\ &+c_{e2}(\dot{z}_{e2} - \dot{q}_1(t) + \frac{\sqrt{2}}{4} l(\dot{\theta}_x(t) + \dot{\theta}_y(t))) + k_{e2}(z_{e2} - q_1(t) + \frac{\sqrt{2}}{4} l(\theta_x(t) + \theta_y(t))) \\ &+c_{f2}(\dot{z}_{f2} - \dot{q}_1(t) - \frac{\sqrt{2}}{4} l(\dot{\theta}_x(t) + \dot{\theta}_y(t))) + k_{f2}(z_{f2} - q_1(t) - \frac{\sqrt{2}}{4} l(\theta_x(t) + \theta_y(t))) - m_1 g = 0 \end{aligned} \tag{20}$$

a) Vibration differential equation of HVTIR body pitching around the X-axis and Y-axis, as shown in Equation (21):

$$\begin{aligned} &J_1\ddot{\theta}_{j(t)} - \frac{\sqrt{2}}{2} lc_{i2}(\dot{z}_{i2} - \dot{q}_1(t) + \frac{\sqrt{2}}{2} l\dot{\theta}_j(t)) - \frac{\sqrt{2}}{2} lk_{i2}(z_{i2} - q_1(t) + \frac{\sqrt{2}}{2} l\theta_j(t)) \\ &+\frac{\sqrt{2}}{2} lc_{h2}(\dot{z}_{h2} - \dot{q}_1(t) + \frac{\sqrt{2}}{2}\dot{\theta}_j(t)) + \frac{\sqrt{2}}{2} lk_{h2}(z_{h2} - q_1(t) + \frac{\sqrt{2}}{2} l\theta_j(t)) \\ &-\frac{1}{2} lc_{e2}(\dot{z}_{e2} - \dot{q}_1(t) + \frac{\sqrt{2}}{4} l(\dot{\theta}_x(t) + \dot{\theta}_y(t))) - \frac{1}{2} lk_{e2}(z_{e2} - q_1(t) + \frac{\sqrt{2}}{4} l(\theta_x(t) + \theta_y(t))) \\ &+\frac{1}{2} lc_{f2}(\dot{z}_{f2} - \dot{q}_1(t) - \frac{\sqrt{2}}{4} l(\dot{\theta}_x(t) + \dot{\theta}_y(t))) + \frac{1}{2} lk_{f2}(z_{f2} - q_1(t) - \frac{\sqrt{2}}{4} l(\theta_x(t) + \theta_y(t))) - M_j = 0 \\ &(i = a, h = c, j = x; i = b, h = d, j = y) \end{aligned} \tag{21}$$

Where M_x is the resultant moment around the X-axis of the robot body subjected to external force, Where M_y is the resultant moment around the Y-axis of the robot body

subjected to external force, and J_l is the moment of inertia of the robot body simplified into a cuboid, as shown in Equation (22):

$$J_1 = \frac{1}{1\,2}(l^2 + h^2) \tag{22}$$

b) Vibration differential equation of two mechanical arms, as shown in Equation (23):

$$\begin{gathered} m_{i2}\ddot{z}_{i2} - c_{i2}(\dot{z}_{i2} - \dot{q}_1(t) - \tfrac{\sqrt{2}}{4}l(\dot{\theta}_x(t) + \dot{\theta}_y(t))) - k_{i2}(z_{i2} - q_1(t) - \tfrac{\sqrt{2}}{4}l(\theta_x(t) + \theta_y(t))) \\ +c_{i2}(\dot{q}_{i1}(t) - \dot{z}_{i2}) + k_{i1}(q_{i1}(t) - z_{i2}) - m_{i2}g = 0 \\ (i = e, j) \end{gathered} \tag{23}$$

c) Vibration differential equation of two landing grippers, as shown in Equation (24):

$$\begin{gathered} m_{i1}\ddot{q}_{i1}(t) - c_{i1}(\dot{q}_{i1}(t) - \dot{z}_{i2}) - k_{i1}(q_{i1}(t) - z_{i2}) + c_{i3}(\dot{z}_l(t) - \dot{z}_{i1}) + k_{i3}(z_l(t) - z_{i1}) - m_{i1}g = 0 \\ (i = e, l = l_x; i = f, l = l_{x+1}) \end{gathered} \tag{24}$$

d) Vibration differential equation of transmission line:

As shown in **Figure 6** and **Figure 9**, the transmission line is treated as n mass segments of 1 meter length, and the vibration differential equation is as follows.

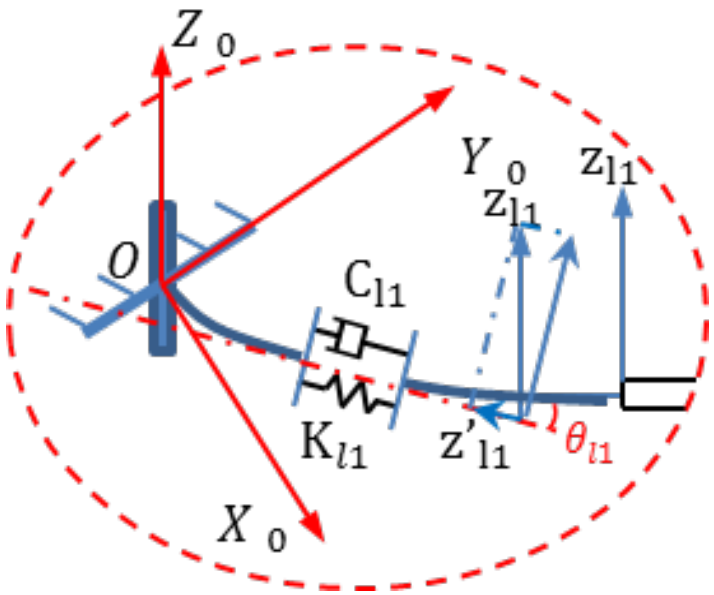

Figure 9. Vibration model at both ends of the transmission line.

The vertical vibration differential equation is shown in Equation (25):

$$\begin{gathered} m_i\ddot{z}_i(t) - c_{i3}(\dot{z}_i - \dot{z}_{i1}) - k_{i3}(z_i - z_{i1}) + c_i\dot{z}_i sin\theta_i + k_l z_l sin\theta_i = 0 \\ (i = e, l = l_x; i = f, l = l_{x+1}) \end{gathered} \tag{25}$$

The differential equation of pitching vibration around the center of mass is as shown in Equation (26):

$$J_2\ddot{\theta}_{xy2(t)} + \frac{1}{2}l_2(c_{f3}(\dot{z}_{f3} - \dot{z}_{f1}) + k_{f3}(z_{f3} - z_{f1})) - \frac{1}{2}l_2(c_{e3}(\dot{z}_{e3} - \dot{z}_{e1}) + \dot{k}_{b3}(z_{e3} - z_{e1})) + \frac{1}{2}l\theta_{f4}(t)(c_{f4}\dot{z}_{f4}\dot{\theta}_{f4}(t) + k_{f4}z_{f4}\theta_{f4}(t)) - \frac{1}{2}l\theta_{f4}(t)(c_{e4}\dot{z}_{e4}\dot{\theta}_{e4}(t) + k_{e4}z_{e4}\theta_{e4}(t)) - M_2 = 0 \quad (26)$$

The vibration differential equation of the HVTIR system is rewritten into matrix form as shown in Equation (27).

$$M_{ALL}\ddot{Z}_{ALL} + C_{ALL}\dot{Z}_{ALL} + K_{ALL}Z_{ALL} = F_{ALL} \quad (27)$$

M_{ALL} is the mass matrix of the vibration system model.

C_{ALL} is the damping matrix of the system.

K_{ALL} is the stiffness matrix of the system.

Z_{ALL} is the vibration displacement matrix.

F_{ALL} is the system force matrix.

The vibration response of the system output can be calculated from the vibration equation matrix.

3. Results and discussion

3.1. Simulation and analysis

This study simplifies the coupled vibration model without considering measurement errors of components, sensor accuracy limitations, parameter changes, airflow disturbances caused by rotor rotation in windless conditions, and the random errors caused by personnel operations.

Due to space limitations, the laboratory has established a reduced version of the transmission line tower system. The tower is made of a welded steel structure with a height of 1.8 m. The transmission line uses 23.8 mm diameter steel-cored aluminum stranded wire with a weight of 1.402 kg/m. The system, with a length of 3 m, is built here. The transmission line is divided into three sections, each of which is 1 m. The system is shown in **Figure 10**.

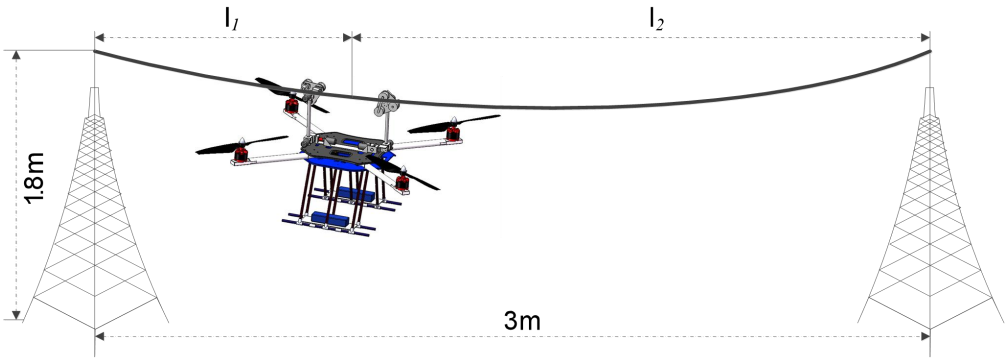

Figure 10. Schematic diagram of the robot-line system.

The mass, size, and torque parameters of the HVTIR are obtained by measuring the physical prototype of the HVTIR. The parameters of the transmission line are calculated according to the location of the landing point, as shown in **Table 1**, where L_1 = 1 m and L_2 = 1 m.

Table 1. HVTIR parameters 1.

Parameter	Description	Value
$m_{a1}/m_{b1}/m_{c1}/m_{d1}$	Rotor component mass	0.2 kg
$m_{a2}/m_{b2}/m_{c2}/m_{d2}$	Rotorcraft arm mass	0.3 kg
m_{e1}/m_{f1}	Gripper component mass	1.2 kg
m_{e2}/m_{f2}	Gripper arm mass	0.8 kg
m_B	HVTIR base mass	6.8 kg
l	Rotorcraft arm length	0.32 m
m_{l1}	Line 1 mass	1.402* l_1 kg
m_{l2}	Line 2 mass	1.402* l_2 kg

The stiffness and damping parameters of the HVTIR and the transmission line are obtained by the finite element analysis method, as shown in **Table 2**.

Table 2. HVTIR parameters 2.

Parameter	Description	Value
$C_{a1}/C_{b1}/C_{c1}/C_{d1}$	Rotor component damping	16 N•s/m
$K_{a1}/K_{b1}/K_{c1}/K_{d1}$	Rotor component stiffness	8,600,000 N/m
$C_{a2}/C_{b2}/C_{c2}/C_{d2}$	Rotorcraft arm damping	56 N•s/m
$K_{a2}/K_{b2}/K_{c2}/K_{d2}$	Rotorcraft arm stiffness	2,350,000 N/m
C_{e1}/C_{f1}	Gripper component damping	485 N•s/m
K_{e1}/K_{f1}	Gripper component stiffness	29,000,000 N/m
C_{e2}/C_{f2}	Gripper arm damping	380 N•s/m
K_{e2}/K_{f2}	Gripper arm stiffness	7,100,000 N/m
C_B	HVTIR base damping	46 N•s/m
K_B	HVTIR base stiffness	35,300,000 N/m
C_{l1}	Line 1 damping	25.963*l_1 N•s/m
K_{l1}	Line 1 stiffness	416330*l_1 N/m
C_{l2}	Line 2 damping	25.963*l_2 N•s/m
K_{l2}	Line 2 stiffness	416330*l_2 N/m

Using the Simulink module of Matlab and according to the transfer function, the coupling vibration model of the system from the rotor component input to the gripper and the transmission line is constructed.

Figure 11 shows the details of the four rotor input forces of the flying HVTIR from the fixed point flight to the stop flight mode during the landing process. The input forces $F_1/F_2/F_3/F_4$ decelerate from 31.85 N to 0 N after 2 S.

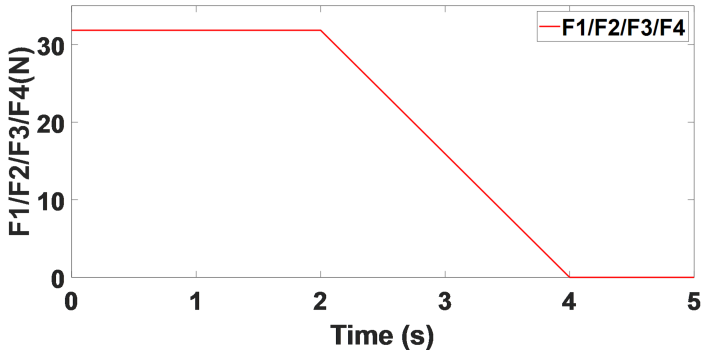

Figure 11. Rotor input force.

It can be seen from **Figures 12** and **13** that after 2 S, the vibration trend of the HVTIR gripper is similar to that of the transmission line coupling point. It can be seen from **Figure 14** that the vibration simulation value of the upper quartile Q3 is 1.54, the lower quartile Q1 is −0.82, and the interquartile range of the interquartile range is 2.36 during the deceleration of the gripper landing; the upper quartile Q3 of the simulation value at the coupling contact of the transmission line is 0.58, the lower quartile Q1 is −0.31, and the interquartile range is 0.89. The normal distribution of the simulation data and the experimental data is centralized, and the two sets of data are in good condition.

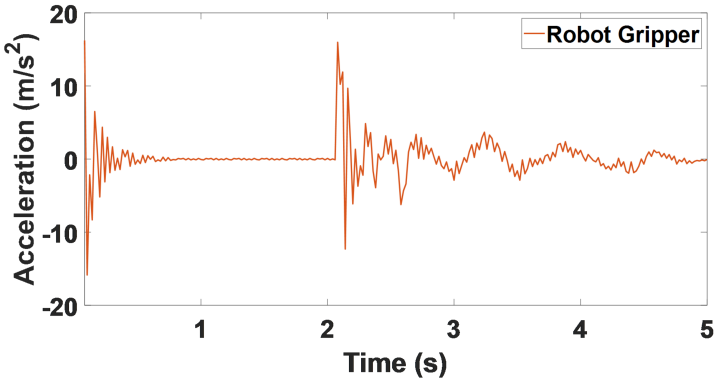

Figure 12. Vibration simulation curve of HVTIR gripper.

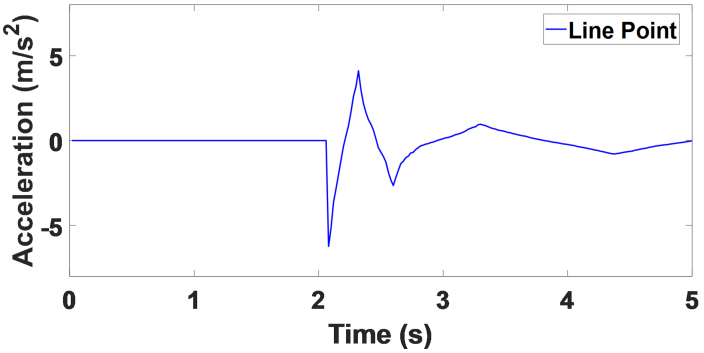

Figure 13. Vibration simulation curve of transmission line coupling point.

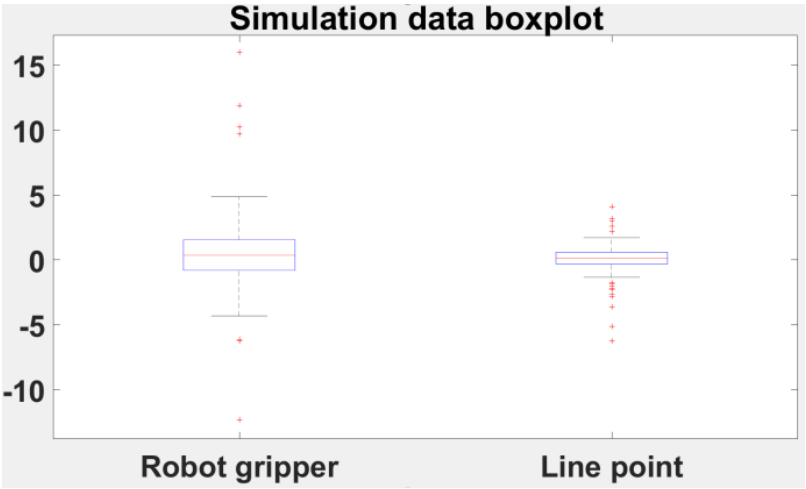

Figure 14. Vibration simulation curve of transmission line coupling point.

3.2. Experiment and discussion

The experiment simulates the landing process, as shown in **Figures 15** and **16**. First, the HVTIR flies to the transmission line at a fixed point, and the HVTIR gripper is ready to contact the transmission line, as shown in **Figure 15**. When the HVTIR lands, the HVTIR gripper contacts with the transmission line, the output tension of the blade is reduced to 0, and finally, the landing is completed, as shown in **Figure 16**. The experimental system uses MPU6050 to measure the input and output vibration acceleration of the system. The system structure is shown in **Figure 16**. Two MPU6050s are fixed near the coupling point of the transmission line, and one MPU6050 is fixed at the center of the gripper. The data adopts an offline real-time acquisition method.

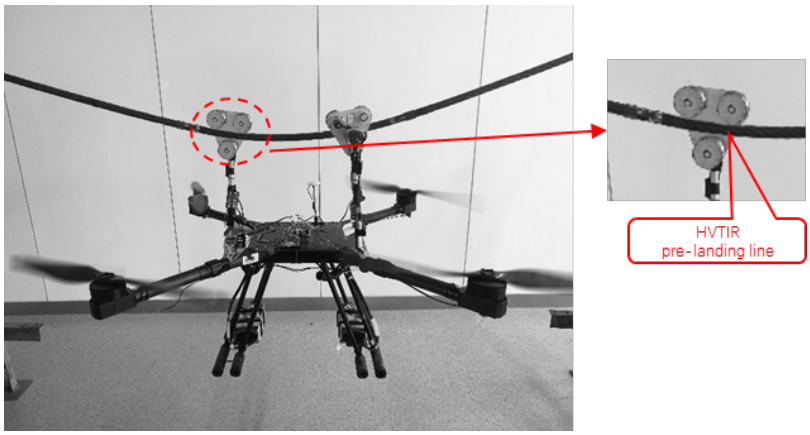

Figure 15. Schematic diagram of HVTIR pre-landing on line.

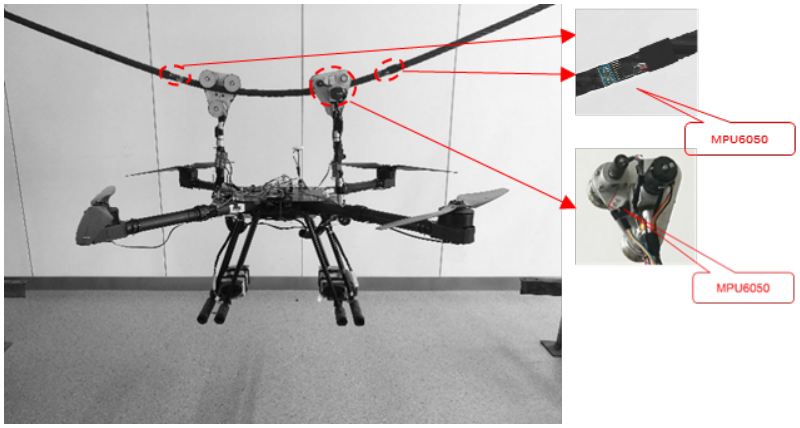

Figure 16. Schematic diagram of HVTIR landing on line, installation position of vibration sensor.

Through experimental data, the vibration characteristics at the coupling point between the HVTIR gripper and the transmission line are obtained as shown in **Figures 17** and **18**.

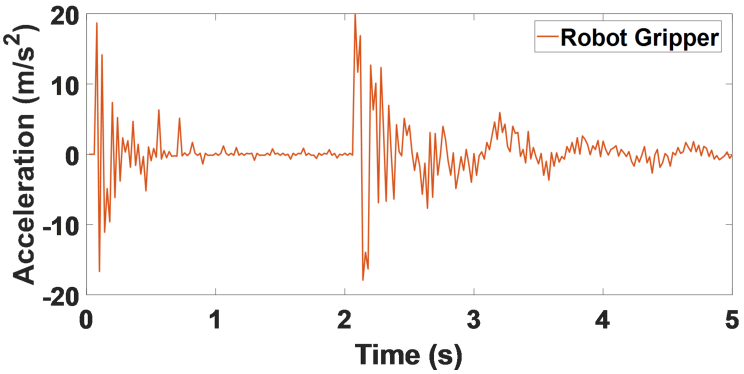

Figure 17. Vibration Experimental curve of the HVTIR gripper.

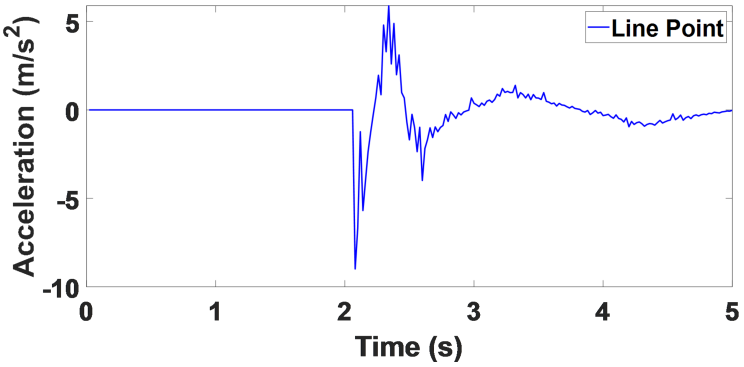

Figure 18. Vibration Experimental curve of transmission line coupling point.

As shown in **Figure 19**, the maximum simulation value of HVTIR gripper vibration is 15.98 m/s^2, the maximum experimental value is 18.16 m/s^2, and the error is 13.64%; the maximum simulation value of vibration at the coupling point of transmission line is −6.23 m/s^2, and the maximum experimental value is −6.62 m/s^2, with an error of 11.08%.

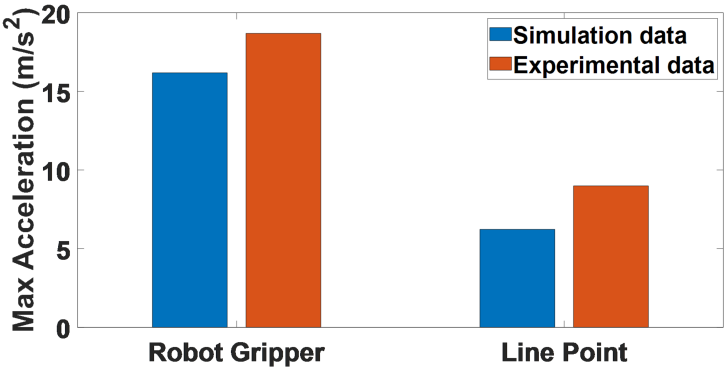

Figure 19. Maximum vibration of the simulation and experiment.

The box diagram of the simulated and experimental values of the vibration at the coupling of the HVTIR gripper and the transmission line is shown in **Figure 20**.

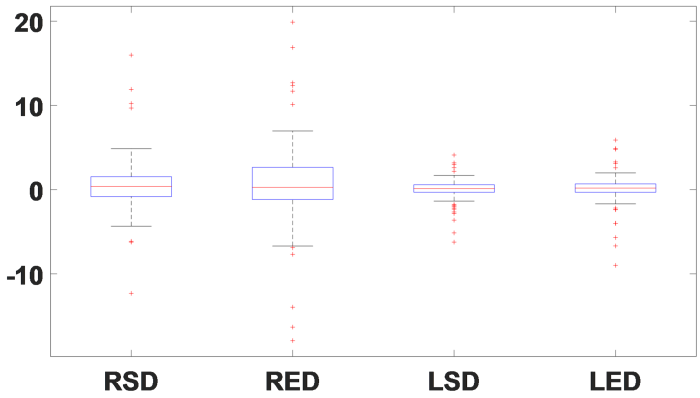

Figure 20. Steady vibration box diagram.

The experimental data of the robot gripper (RED) during the deceleration of landing is 2.65 in the upper quartile Q3, −1.17 in the lower quartile Q1, and 3.82 in the interquartile range; the simulation data of the robot gripper (RSD) of the upper quartile Q3 is 2.31, the lower quartile Q1 is −0.92, and the interquartile range is 3.23, an increase of 18.26%.

The experimental data at coupling point of transmission line (LED) during deceleration is 0.68 in the upper quartile Q3, −0.31 in the lower quartile Q1, and 0.99 in the interquartile range; the simulation data at coupling point of transmission line (LSD) of the upper quartile Q3 is 0.58, the lower quartile Q1 is −0.31, and the interquartile range is 0.89, an increase of 10.67% (**Table 3**).

Table 3. Numerical analysis table.

State	Max	Max Ratio	(Q1, Q3)	IR	IR Ratio
RSD	15.98	13.64%	(−0.92, 2.31)	3.23	18.26%
RED	19.89		(−1.17, 2.65)	3.82	
LSD	6.23	11.08%	(−0.31, 0.58)	0.89	10.67%
LED	6.92		(−0.31, 0.68)	0.99	

As shown in **Figures 21** and **22**, the simulation values of the vibration acceleration at the coupling point between the robot wheel claw and the power transmission line are highly consistent with the Quantile-Quantile distribution of the experimental values. This demonstrates the scientific validity of the simulation model.

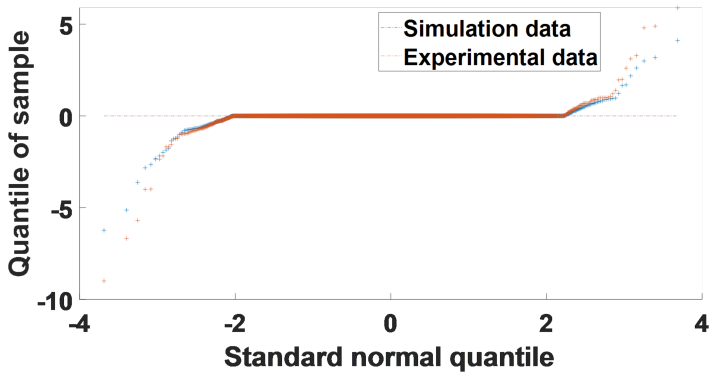

Figure 21. Quantile-Quantile of Robot Gripper (Sample data-Standard Normal).

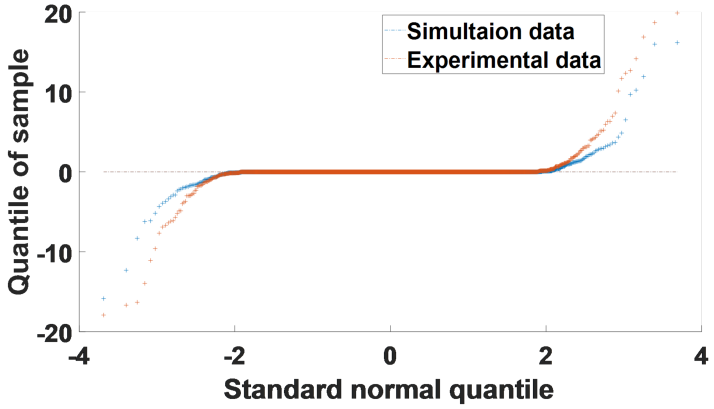

Figure 22. Quantile-Quantile of Landing Line point (Sample data-Standard Normal).

It is found by comparison that the maximum error between the RSD and RED during the HVTIR landing is not more than 13.64%. Although the interquartile spacing in the box diagram has increased by 18.26%, its numerical concentration is good, and the normal distribution is basically consistent. The maximum error between the LED and LSD is not more than 11.08%. In the box diagram, the values are concentrated, and the interquartile spacing increases by no more than 10.67%, and the consistency of the normal distribution of Quantile-Quantile is good, which proves the scientific consistency of the experiment and simulation.

4. Discussion

The purpose of this article is to obtain the law of coupling vibration between robots and power lines during the HVTIR landing process. Therefore, this paper uses the method of theoretical model and experiment to analyze the coupling vibration characteristics of the HVTIR and the transmission line in landing flight; the results are as follows:

(a) Comparing the experimental data with the model simulation data, it is found that the vibration trend of the HVTIR gripper is similar, the numerical value is relatively concentrated, and the maximum increase of vibration is not more than 13.64%. In the box plot, the interquartile spacing at the contact point increases by 10.67%. The error range is basically reasonable. The reason for such errors is that the simplified model did not take into account factors such as measurement errors of component quality, stiffness, and damping; measurement accuracy of MPU6050; and random errors of operators.

(b) Comparing the experimental data with the model simulation data, it is found that the vibration trend of the transmission line is similar, the numerical value is relatively concentrated, and the maximum increase of vibration is not more than 11.08%. In the box plot, the interquartile spacing at the contact point of transmission ne increases by 10.67%. The error range is reasonable. This proves the rationality of the transmission line model. The reason for the error is the measurement error of the transmission line and the measurement accuracy of the MPU6050.

(c) The research on model simulation and experiment shows that the rigid-flexible

coupling vibration model of HVTIR during landing is reasonable. The main reason for the occurrence of errors is that the model did not consider factors such as measurement errors, sensor accuracy, and random errors of operators. Subsequent research can incorporate measurement errors, sensor accuracy, and parameter changes into the model. It is possible to reduce data errors through multiple measurements, reduce random errors of operators through multiple experiments, and obtain corresponding patterns of error changes through changes in the size of transmission lines.

5. Conclusion

This article studies the characteristics of transmission lines and constructs a transmission line model with stiffness and damping links between multiple unit beams; constructs a stiffness-damping coupling model for the contact force between the robot gripper and the power transmission line. By analyzing the dynamics of each component, a rigid-flexible coupling vibration model of the robot and the power transmission line during the robot landing process was ultimately constructed. The coupling law between the robot and the line is obtained. The scientific effectiveness of the established rigid-flexible coupling model has been demonstrated through simulation and experimental comparison.

Author contributions: Conceptualization, XZ and HS; methodology, HS; software, HS and ABA; validation, HS, XZ and HX; formal analysis, HS and ABA; investigation, XZ, HS, ABA and HX; resources, HS and ABA; data curation, XZ and HS; writing—original draft preparation, XZ and HS; writing—review and editing, XZ and HS; visualization, XZ and HS; supervision, HX and HS; project administration, XZ and HX; funding acquisition, XZ and HX. All authors have read and agreed to the published version of the manuscript.

Funding: This research was funded by the Key Research and Development Plan of Shaanxi Province, China, grant number 2018ZDXM-GY-093.

Institutional review board statement: Not applicable.

Informed consent statement: Not applicable.

Data availability statement: Not applicable.

Conflict of interest: The authors declare no conflict of interest.

References

1. Alhassan AB, Zhang X, Shen H, et al. Power transmission line inspection robots: A review, trends and challenges for future research. International Journal of Electrical Power & Energy Systems. 2020; 118: 105862. doi: 10.1016/j.ijepes.2020.105862
2. Liu Y, Li X, Qiao R, et al. Lightweight Insulator and Defect Detection Method Based on Improved YOLOv8. Applied Sciences. 2024; 14(19): 8691. doi: 10.3390/app14198691
3. Li Y, Zou G, Zou H, et al. Insulators and Defect Detection Based on the Improved Focal Loss Function. Applied Sciences. 2022; 12(20): 10529. doi: 10.3390/app122010529

4. Chen D-Q, Guo X-H, Huang P, et al. Safety Distance Analysis of 500kV Transmission Line Tower UAV Patrol Inspection. IEEE Letters on Electromagnetic Compatibility Practice and Applications. 2020; 2(4): 124–128. doi: 10.1109/LEMCPA.2020.3040878
5. Wang Y, Qin X, Jia W, et al. Multiobjective Energy Consumption Optimization of a Flying–Walking Power Transmission Line Inspection Robot during Flight Missions Using Improved NSGA-II. Applied Sciences. 2024; 14(4): 1637. doi: 10.3390/app14041637
6. Luo Y, Yu X, Yang D, et al. A survey of intelligent transmission line inspection based on unmanned aerial vehicle. Artificial Intelligence Review. 2023; 56(1): 173–201. doi: 10.1007/s10462-022-10189-2
7. Chao C, Mei X, Wei Y, et al. A balanced walking-clamp mechanism for inspection robot of transmission line. Industrial Robot: the international journal of robotics research and application. 2023; 50(4): 673–685. doi: 10.1108/IR-09-2022-0226
8. Shruthi CM, Sudheer AP, Joy ML. Dual arm electrical transmission line robot: motion through straight and jumper cable. Automatika. 2019; 60(2): 207–226. doi: 10.1080/00051144.2019.1609256
9. Yue X, Wang H, Feng Y, et al. Improving Stability of Line Inspection Robot During Crossing Jumper Lines With a Centroid Adjustment Adjusting Mechanism. IEEE Access. 2022; 10: 134571–134579. doi: 10.1109/ACCESS.2022.3228386
10. Li Z, Tian Y, Yang G, et al. Vision-Based Autonomous Landing of a Hybrid Robot on a Powerline. IEEE Transactions on Instrumentation and Measurement. 2023; 72: 1–11. doi: 10.1109/TIM.2022.3224524
11. Zheng X, Wu G, Jiang W, et al. Rigid–Flexible Coupling Dynamics with Contact Estimator for Robot/PTL System. Proceedings of the Institution of Mechanical Engineers, Part K: Journal of Multi-body Dynamics. 2020; 234(4): 635–649. doi: 10.1177/1464419320933382
12. Jia W, Lei J, Qin X, et al. Dynamic Modeling and Analysis of a Flying–Walking Power Transmission Line Inspection Robot Landing on Power Transmission Line Using the ANCF Method. Applied Sciences. 2025; 15: 1863. doi: 10.3390/app15041863
13. Alhassan AB, Zhang X, Shen H, et al. Precise Motion Control of a Power Line Inspection Robot Using Hybrid Time Delay and State Feedback Control. Frontiers in Robotics and AI. 2022; 9: 746991. doi: 10.3389/frobt.2022.746991
14. Ye X, Cui H, Wang L, et al. Vision-Guided Hierarchical Control and Autonomous Positioning for Aerial Manipulator. Applied Sciences. 2023; 13(22): 12172. doi: 10.3390/app132212172
15. Luna AL, Cortés HR, Vega IC, et al. An Immersion and Invariance Controller for Aerial Manipulation. Unmanned Systems. 2022; 10(04): 343–353. doi: 10.1142/S2301385022410023
16. Yigit A, Perozo MA, Cuvillon L, et al. Novel Omnidirectional Aerial Manipulator With Elastic Suspension: Dynamic Control and Experimental Performance Assessment. IEEE Robotics and Automation Letters. 2021; 6(2): 612–619. doi: 10.1109/LRA.2020.3048880
17. Ji M, Shen J, Cao H, et al. Avian-inspired high-precision tracking control for aerial manipulators. Nonlinear Dynamics. 2025; 113(8): 8605–8621. doi: 10.1007/s11071-024-10584-0
18. Hamaza S, Georgilas I, Richardson T. Towards an Adaptive-Compliance Aerial Manipulator for Contact- Based Interaction. In: Proceedings of the 2018 IEEE/RSJ International Conference on Intelligent Robots and Systems (IROS); 1–5 October 2018; Madrid, Spain. pp. 1–9. doi: 10.1109/IROS.2018.8593576
19. Zhang Z, Chen Y, Wu Y, et al. Gliding grasping analysis and hybrid force/position control for unmanned aerial manipulator system. ISA Transactions. 2022; 126: 377–387. doi: 10.1016/j.isatra.2021.07.038
20. Khanmirza E, Daneshjou K, Ravandi AK. Underactuated Flexible Aerial Manipulators: a New Framework for Optimal Trajectory Planning Under Constraints Induced by Complex Dynamics. Journal of Intelligent & Robotic Systems. 2018; 92(3–4): 599–613. doi: 10.1007/s10846-017-0711-6
21. Meng X, He Y, Han J. Hybrid Force/Motion Control and Implementation of an Aerial Manipulator towards Sustained Contact Operations. In: Proceedings of the 2019 IEEE/RSJ International Conference on Intelligent Robots and Systems (IROS); 3–8 November 2019; Macau, China. pp. 3678–3683. doi: 10.1109/IROS40897.2019.8967808
22. Wang T, Umemoto K, Endo T, et al. Modeling and Control of a Quadrotor UAV Equipped With a Flexible Arm in Vertical Plane. IEEE Access. 2021; 9: 98476–98489. doi: 10.1109/ACCESS.2021.3095536
23. Zhang X, Shen H, Alhassan AB, et al. Gripper vibration analysis of inspection robot during variable working flight of pre-landing on high-voltage transmission line. Journal of Mechanical Science and Technology. 2024; 38(3): 1411–1428. doi: 10.1007/s12206-024-0233-7

24. Daisy M, Dashti R, Shaker HR, et al. Fault location in power grids using substation voltage magnitude differences: A comprehensive technique for transmission lines, distribution networks, and AC/DC microgrids. Measurement. 2023; 220: 113403. doi: 10.1016/j.measurement.2023.113403
25. Li Z, Zhang Y, Wu H, et al. Design and Application of a UAV Autonomous Inspection System for High-Voltage Power Transmission Lines. Remote Sensing. 2023; 15(3): 865. doi: 10.3390/rs15030865